Pergamon

PII: S0148-9062(97)00307-0

Int. J. Rock Mech. Min. Sci. Vol. 34, No. 8, pp. 1187–1199, 1997

Printed in Great Britain
0148-9062/97 $17.00 + 0.00

Evaluation of Fully-Coupled Strata Deformation and Groundwater Flow in Response to Longwall Mining

JUN-MO KIM†‡
R. R. PARIZEK†
D. ELSWORTH§

A finite element poroelastic model is presented to evaluate fully-coupled strata deformation and groundwater flow resulting from underground longwall mining in variably saturated fractured geologic media through an equivalent porous elastic continuum representation. The explicit coupling between the groundwater flow field and the solid skeleton deformation field is achieved by simultaneously solving the governing equations for groundwater flow and solid skeleton deformation. The implicit coupling between these two fields is also accomplished by considering the effects of both unsaturated water flow and solid skeleton deformation on the hydraulic properties such as water content and hydraulic conductivity. In addition to the implicit coupling caused by unsaturated water flow, the other implicit coupling caused by solid skeleton deformation is also important because it may produce hydraulic heterogeneity and anisotropy in a geologic medium affecting the groundwater flow field even when the system is in a fully saturated condition. A physically based constitutive model is proposed to account for the deformation (strain)-dependencies of porosity and saturated hydraulic conductivity of the fractured media. To evaluate the impacts of longwall mining and to understand their hydrogeomechanical nature, the numerical model is applied to a well documented case study with satisfactory results. Although the numerical simulation results presented in this paper will not apply to all underground longwall mines because of differences in site-specific hydrogeological and geomechanical settings, the methodology described herein may find some useful applications in many longwall mining projects. © 1998 *Elsevier Science Ltd*

INTRODUCTION

A variety of field studies have documented the environmental impacts of longwall mining (rapid and high extraction ratio underground coal mining) including land subsidence, depressurization of aquifers, and severe modification of hydraulic properties [1–7]. These studies also show that such longwall mining-induced impacts arise not only from the drainage of groundwater into mined panels (hydraulic stress) but also from the changes in the overburden stress regime (mechanical stress). In other words, longwall mining disrupts the pre-existing hydraulic and mechanical equilibrium conditions in fractured geologic media creating fully-coupled strata deformation and groundwater flow taking place simultaneously. The increasing use of coal as an energy source has prompted the need for a better understanding of hydrogeological and geomechanical behavior of the geologic media associated with longwall mining. Such knowledge may provide some useful guidelines for controlling and minimizing the longwall mining-induced adverse environmental impacts.

Numerical methods (e.g. finite difference and finite element methods) have emerged as powerful tools for predicting and analyzing hydrogeological and geomechanical problems in a wide range of environments (e.g. mining, excavation, surface loading, pumping, and drainage). These methods permit complex geometry, various boundary conditions, non-linear material behavior, heterogeneity as well as anisotropy to be considered. Various numerical studies have been performed in modelling longwall mining-induced groundwater flow [8–11] or land subsidence [12–16] based on the

---

†Department of Geosciences, Deike Building, Pennsylvania State University, University Park, PA 16802, U.S.A.

‡Corresponding author; currently at Department of Geological Sciences, Seoul National University, Seoul 151-742, Korea.

§Department of Mineral Engineering, Hosler Building, Pennsylvania State University, University Park, PA 16802, U.S.A.

conventional theory of groundwater flow or solid skeleton deformation by decoupling the groundwater flow field from the solid skeleton deformation field. However, such approaches may not be rigorous because longwall mining intrinsically induces the hydraulic–mechanical interaction between these two fields. This fully-coupled phenomenon can be better understood through the theory of poroelasticity [17–20], which explains groundwater flow through deforming variably saturated geologic media. In this theory, a simultaneous solution is sought for the pore water pressure and both vertical and horizontal displacements taking place simultaneously in a three-dimensional system. Thus poroelastic theory makes it possible to provide a more rigorous and realistic treatment of the hydrogeomechanical behavior of deforming geologic media. On the basis of poroelastic theory, several numerical studies have been conducted in modelling longwall mining-induced solid deformation and its effects on hydraulic conductivity and groundwater flow within saturated geologic media [21–25]. However, unsaturated groundwater flow was not considered in these numerical studies. In addition, the solid skeleton deformation field and the groundwater flow field were actually uncoupled and solved sequentially in most cases [21,23–25].

This paper presents a general multidimensional finite element model to simulate fully-coupled strata deformation and groundwater flow in variably saturated fractured geologic media. In addition, a physically based constitutive model is proposed to account for the deformation (strain)-dependencies of porosity and saturated hydraulic conductivity of the fractured media. To evaluate the impacts of longwall mining and to understand the basic processes, the numerical model is validated against a well documented case study. The basic assumption underlying this study is that the fractured rock mass behaves as an equivalent porous elastic continuum with interconnected fractures dominating the groundwater flow and strata deformation patterns [26–28]. The obvious advantage of treating fractured geologic media as equivalent continua is that the governing equations for groundwater flow and solid skeleton deformation, which have been developed for porous media, can be applied directly, and no additional assumptions and parameters are involved. This equivalent porous elastic continuum representation is also convenient since it enables changes in porosity and hydraulic conductivity that result from strata deformation to be straightforwardly evaluated by using body (rock mass) strains.

FRAMEWORK OF HYDROGEOMECHANICAL MODEL

A general hydrogeomechanical model describing saturated–unsaturated groundwater flow in deforming geologic media may be formulated by fully, i.e. explicitly and implicitly, coupling the groundwater flow field and the solid skeleton (medium) deformation field. The explicit coupling between these two fields can be achieved by simultaneously solving the mathematical equations governing groundwater flow and solid skeleton deformation. The implicit coupling between these two fields can also be accomplished by accounting for the effects of both unsaturated water flow and solid skeleton deformation on the hydraulic properties such as water content and hydraulic conductivity.

Governing equations

The governing equations for groundwater flow in a deformable variably saturated geologic medium can be derived based on the following basic assumptions: (1) the geologic medium is porous and elastic, while individual solid grains are incompressible, (2) saturated–unsaturated fluid flow follows Darcy's law, and (3) Hooke's law holds for elastic deformation of the geologic medium. These governing equations may be written as [17–20]:

$$\nabla\cdot[-\mathbf{K}\cdot\nabla(h+z)] + \left(n\frac{\mathrm{d}S_w}{\mathrm{d}h} + nS_w\beta_w\gamma_w\right)\frac{\partial h}{\partial t} + S_w\frac{\partial}{\partial t}\left(\frac{\partial u_k}{\partial x_k}\right) = q \quad (1)$$

$$\frac{\partial}{\partial x_j}\left[G\left(\frac{\partial u_i}{\partial x_j} + \frac{\partial u_j}{\partial x_i}\right) + \lambda\left(\frac{\partial u_k}{\partial x_k}\right)\delta_{ij} - (S_w\gamma_w h\delta_{ij})^e\right] + [nS_w\rho_w + (1-n)\rho_s]^e g_i = 0 \quad i,j = x,y,z \quad (2)$$

In equation (1), $\mathbf{K}$ is the effective hydraulic conductivity tensor, $h = P/\gamma_w$ is the pressure head, z is the elevation head, n is the porosity, S_w is the degree of water saturation, β_w is the compressibility of water, $\gamma_w = \rho_w g$ is the unit weight of water, u_k is the displacement of a solid in the k direction, q is the fluid source(+)/sink(−) term, and t is time. Here P is the pore water pressure (positive for compression), ρ_w is the density of water, and g is the gravitational acceleration constant. Note that $\phi = h + z$ is the hydraulic head, $\mathrm{d}S_w/\mathrm{d}h$ is the specific saturation capacity, $\theta_w = nS_w$ is the water content, and $\epsilon_v = \partial u_k/\partial x_k$ is the volumetric strain. In addition, $\mathbf{q}_r = -\mathbf{K}\cdot\nabla(h+z)$ is the Darcy velocity (flux). In equation (2), $G = E/2(1+v)$ is the shear modulus, $\lambda = Ev/(1+v)(1-2v)$ is the Lamé's constant, E is Young's modulus (=effective rock mass modulus E_{mass}), v is Poisson's ratio, δ_{ij} is the Kronecker's delta (1 if $i = j$, and 0 if $i \neq j$), ρ_s is the solid density, and g_i is the component of gravitational acceleration in the i direction. The superscript e in equation (2) denotes the incremental values of physical quantities. For example, $h^e = h - h^o$ is the incremental pressure head in which h and h^o are the current and initial pressure heads, respectively. On the left hand side of equation (2), the sum of three terms in the square bracket is equal to the incremental total stress tensor σ_{ij}^e (positive for tension), while the sum of the first two terms is equal to the deformation-producing incremental effective stress tensor $\sigma_{ij}'^e$ (positive for tension). The last term on the left hand side of equation (2) also represents the incremental body force f_i^e.

Meanwhile, for variably saturated deforming media, the water content θ_w and effective hydraulic conductivity tensor **K** in equations (1) and (2) may be considered functions of both pore water pressure P and incremental effective stress tensor $\sigma_{ij}^{\prime e}$ or, in turn, functions of pressure head h and resulting strain tensor ϵ_{ij} as follows:

$$\theta_w = \theta_w(P, \sigma_{ij}^{\prime e}) = \theta_w(h, \epsilon_{ij}) = S_w(h)n(\epsilon_{ij}) \qquad (3)$$

$$\mathbf{K} = \mathbf{K}(P, \sigma_{ij}^{\prime e}) = \mathbf{K}(h, \epsilon_{ij}) = K_r(h)\mathbf{K}_{sat}(\epsilon_{ij}) \qquad (4)$$

where K_r is the relative hydraulic conductivity, and $\mathbf{K}_{sat}$ is the saturated hydraulic conductivity tensor. In deriving equations (3) and (4), it is assumed that the unsaturated hydraulic properties (S_w and K_r) are unique functions of the pressure head, whereas the saturated hydraulic properties (n and $\mathbf{K}_{sat}$) are unique functions of the strain tensor.

Effect of unsaturated water flow on unsaturated hydraulic properties

In an unsaturated flow condition where the pressure head h becomes negative or less than an air-entry value, the water saturation S_w and relative hydraulic conductivity K_r become dependent upon the pressure head as described in equations (3) and (4). To consider these relationships for porous media, various physical models [29–31] have been developed based on experiments and theories. Peters *et al.* [32] and Reitsma and Kueper [33] applied Brooks and Corey's [29] and Van Genuchten's [30] models to fractured media and showed that these models can also be used in characterizing unsaturated water flow in fractured media as well as in porous media. The following constitutive mathematical relationships can also be used for fractured media to consider the changes in unsaturated hydraulic properties under an unsaturated flow condition [34]:

$$S_w = 1 - (1 - S_{wr})\frac{h - h_a}{h_b - h_a} \quad h_b < h < h_a \qquad (5)$$

$$K_r = \left[1 - (1 - S_{wr})\frac{h - h_a}{h_b - h_a} - S_{wr}\right] \times (1 - S_{wr})^{-1} \quad h_b < h < h_a \qquad (6)$$

where S_{wr} is the residual water saturation, h_a is the air-entry value or bubbling pressure head, and h_b is the allowed minimum pressure head. The specific saturation capacity term $\mathrm{d}S_w/\mathrm{d}h$ in equation (1) can be obtained by differentiating equation (5) with respect to the pressure head h.

On the other hand, the change in water saturation due to the unsaturated water flow gives rise to the change in degree of coupling between the groundwater flow field and the solid skeleton deformation field and the change in body force as described in the governing equations (1) and (2). Thus the unsaturated water flow induces a non-linear implicit coupling across the groundwater flow and solid skeleton deformation fields.

Effect of solid skeleton deformation on saturated hydraulic properties

In deforming geologic media, the porosity and saturated hydraulic conductivity are not constant but are changed by the deformation of solid skeleton as described in equations (3) and (4). Several experimental studies have shown that the aperture (opening) and spacing of a fracture and its saturated hydraulic properties change as a function of normal stress or strain acting on it [35–39]. Thus the deformation of solid skeleton induces another non-linear implicit coupling across the groundwater flow and solid skeleton deformation fields. When the media are fully saturated, this effect becomes more important because the water content and hydraulic conductivity become unique functions of incremental effective stress or resultant strain, and hence heterogeneity and anisotropy of such hydraulic properties may be produced in the media affecting the groundwater flow field. In addition, the change in porosity due to the solid skeleton deformation gives rise to the change in the body force as described in equation (2). A physically based constitutive model is proposed here to account for such deformation (strain)-dependencies of porosity and saturated hydraulic conductivity of the fractured media.

The basic equation of the elastic deformation of a rock mass as a two-component (matrices and fracture sets) system in the direction perpendicular to the fracture sets is derived as follows. A fracture set is defined here as a set of fractures that have the same orientation (strike and dip) and uniform fracture spacing and aperture. Considering a rock mass between centerlines of two adjacent fractures in a fracture set, the rock mass (body) displacement u_{tn} which is normal to the fracture set is the summation of the displacements in the matrix and fractures as:

$$u_{tn} = u_{mn} + u_{fn} \qquad (7)$$

where u_{mn} is the rock matrix normal displacement bounded between the two fractures, u_{fn} is the fracture normal displacement in the fractures, and the subscript n denotes the direction normal to the fracture set. By the definition of strain, equation (7) becomes:

$$s_o\epsilon_{tn} = (s_o - b_o)\epsilon_{mn} + b_o\epsilon_{fn} \qquad (8)$$

where ϵ_{tn} is the average rock mass strain, ϵ_{mn} is the rock matrix strain, ϵ_{fn} is the fracture strain, which are also normal to the fracture set, s_o is the initial fracture spacing, and b_o is the initial fracture aperture. From Hooke's law for a rock mass, equation (8) can be rearranged as [40]:

$$\frac{s_o\sigma_n^{\prime e}}{E_{mass}} = \frac{(s_o - b_o)\sigma_n^{\prime e}}{E_{matrix}} + \frac{\sigma_n^{\prime e}}{k_n} \qquad (9)$$

where $\sigma_n^{\prime e}$ is the incremental effective stress acting normal to the fracture set, E_{mass} is the effective rock mass modulus, E_{matrix} is the rock matrix modulus, and

$k_n = E_{\mathrm{matrix}}\xi/b_o$ is the normal fracture stiffness in which ξ is the normalized mineral contact area on the fracture wall. In deriving equation (9), it is assumed that the incremental effective stresses are in local equilibrium. In other words, the incremental effective stresses in the rock matrix, in the fractures, and hence in the rock mass are identical. Using equations (8) and (9), the fracture normal displacement u_{fn} in equation (7) can be expressed as:

$$u_{fn} = \left[\frac{s_o}{E_{\mathrm{mass}}} - \frac{(s_o - b_o)}{E_{\mathrm{matrix}}}\right]\sigma_n'^{e} = [s_o - (s_o - b_o)R_m]\epsilon_{tn} \quad (10)$$

where $R_m = E_{\mathrm{mass}}/E_{\mathrm{matrix}} = s_o k_n/[(s_o - b_o)k_n + E_{\mathrm{matrix}}]$ represents the modulus reduction ratio which controls the partitioning of the rock mass normal strain ϵ_{tn} between the rock matrix and fractures. Theoretically, the modulus reduction ratio R_m varies between zero and unity. When $R_m = 1$, the rock mass normal strain ϵ_{tn} is uniformly distributed between fractures and matrix resulting in the smallest changes in fracture porosity and saturated hydraulic conductivity. When $R_m \to 0$, the strain is applied entirely to the fracture system and precipitates the largest possible changes in fracture porosity and saturated hydraulic conductivity. The modulus reduction ratio R_m may be readily evaluated from a variety of rock mass classification systems such as the Geomechanics Classification or the Rock Mass Rating (RMR) system developed by Bieniawski [41]. Since the deformability of a rock mass depends directly on the fracture frequency $I\,(=1/s)$, the fracture spacing s as one of six parameters utilized in the Rock Mass Rating (RMR) system may be used in determining the modulus reduction ratio R_m [23]. This method avoids the difficulty of defining a value of the modulus reduction ratio R_m that is unlikely to be available in practice. The rock mass normal strain ϵ_{tn} in equation (10) can be obtained from a global strain tensor by coordinate transformation from global coordinates to local coordinates of the fracture set using direction cosines. The direction cosines can be calculated from strike and dip of the fracture set [42,43].

The deformation-dependent fracture porosity n_j of a fracture set j can be expressed using equations (7), (8), and (10) as:

$$n_j = \frac{b_j}{s_j} = \frac{b_{oj} + u_{fnj}}{s_{oj} + u_{tnj}} = \left\{\frac{b_{oj}}{s_{oj}} + \left[1 - \left(1 - \frac{b_{oj}}{s_{oj}}\right) \times R_{mj}\right]\epsilon_{tnj}\right\}(1 + \epsilon_{tnj})^{-1} \quad (11)$$

where the subscripts j and o denote the fracture set index and the initial values of physical quantities, respectively. Note that $n_{oj} = b_{oj}/s_{oj}$ is the initial fracture porosity of the jth fracture set before the deformation takes place. Considering fracture intersection, the total fracture porosity n of a fractured medium consisting of k fracture sets may then be expressed as follows:

$$\begin{aligned} n = {} & \sum_{j=1}^{k} n_j - n_2 \sum_{j=1}^{1} n_j - n_3 \sum_{j=1}^{2} n_j - \cdots - n_k \sum_{j=1}^{k-1} n_j \\ & + \frac{1}{2}\left(n_3 \sum_{\substack{i,j=1 \\ i \neq j}}^{2} n_i n_j + n_4 \sum_{\substack{i,j=1 \\ i \neq j}}^{3} n_i n_j \right. \\ & \left. + \cdots + n_k \sum_{\substack{i,j=1 \\ i \neq j}}^{k-1} n_i n_j \right) \end{aligned} \quad (12)$$

where it is assumed that the probability that more than three fractures intersect at the same point is zero.

The equivalent saturated hydraulic conductivity K_{sat} in the direction parallel to a planar fracture set j is related to its fracture spacing s_j and fracture aperture b_j as [44,45]:

$$K_{\mathrm{sat}_j} = \frac{\rho_w g}{\mu_w}\frac{1}{12}\frac{b_j^3}{s_j} = \frac{\rho_w g}{\mu_w}\frac{1}{12}\frac{(b_{oj} + u_{fnj})^3}{s_{oj} + u_{tnj}} \quad (13)$$

where K_{sat_j} is the equivalent saturated hydraulic conductivity of the jth fracture set, and μ_w is the dynamic viscosity of water. Substituting equations (7), (8), and (10) into equation (13) gives:

$$K_{\mathrm{sat}_j} = K_{\mathrm{sat}_{oj}}\left\{1 + \left[\frac{s_{oj}}{b_{oj}} - \left(\frac{s_{oj} - b_{oj}}{b_{oj}}\right)R_{mj}\right]\epsilon_{tnj}\right\}^3 \times (1 + \epsilon_{tnj})^{-1} \quad (14)$$

where $K_{\mathrm{sat}_{oj}}$ is the initial equivalent saturated hydraulic conductivity of the jth fracture set before the deformation takes place. The global deformation-dependent equivalent saturated hydraulic conductivity tensor $\mathbf{K}_{\mathrm{sat}}$ of a fractured medium consisting of k fracture sets may then be calculated from equation (14) using coordinate transformation and summation for each fracture set as:

$$\mathbf{K}_{\mathrm{sat}} = \sum_{j=1}^{k} \mathbf{K}_{\mathrm{sat}_j} = \sum_{j=1}^{k} \mathbf{R}_j^T \bar{\mathbf{K}}_{\mathrm{sat}_j} \mathbf{R}_j \quad (15)$$

where $\mathbf{R}_j$ is the rotation matrix from global coordinates to local coordinates of the jth fracture set, $\mathbf{K}_{\mathrm{sat}_j}$ is the global deformation-dependent equivalent saturated hydraulic conductivity of the jth fracture set, $\bar{\mathbf{K}}_{\mathrm{sat}_j}$ is the local deformation-dependent equivalent saturated hydraulic conductivity tensor of the jth fracture set which is equivalent to equation (14), and the superscript T stands for matrix transpose. Here the rotation matrix $\mathbf{R}_j$ for the jth fracture set can also be obtained from the direction cosines [42,43].

As shown in equations (11) and (14), if a fracture is under normal extension (i.e. $\epsilon_{tn} > 0$), its porosity and saturated hydraulic conductivity increase, and *vice versa*. Comparing equation (11) with equation (14), it is also recognized that the equivalent saturated hydraulic conductivity of a fracture set is more sensitive to the deformation of solid skeleton, which is expressed here by the rock mass normal strain ϵ_{in}, than its fracture porosity.

FINITE ELEMENT FORMULATION

As mentioned above, the governing equations (1) and (2) constitute a general mathematical statement of the physical problem of fully-coupled hydraulic–mechanical phenomena in variably saturated geologic media. Unfortunately, a general analytical solution for this problem does not exist. Numerical methods are the only tools that can be used to achieve the general solution for such a general problem. The Galerkin finite element method [46,47] is chosen here to approximate these governing equations because of its ability to treat heterogeneous and anisotropic regions with complex boundaries.

In the Galerkin finite element method, an unknown variable φ, which represents the pressure head h and the displacements u_x, u_y, and u_z in the governing equations (1) and (2), can be approximated by a trial solution $\hat{\varphi}$ in space by means of the basis (shape) functions and their nodal values:

$$\varphi(x, y, z, t) \approx \hat{\varphi}(x, y, z, t)$$

$$= \sum_{J=1}^{NN} N_J(x, y, z)\varphi_J(t) \quad \varphi = h, u_x, u_y, u_z \quad (16)$$

where N_J is the basis function for node J, φ_J is the value of φ at node J, and NN is the total number of nodes in the region of interest. Substitution of equation (16) into equations (1) and (2) and application of Galerkin's principle yields the following matrix equations:

$$\int_R \nabla N_I \cdot \mathbf{K} \cdot \nabla N_J \, \mathrm{d}R\{h\} + \int_R N_I \left(n \frac{\mathrm{d}S_{\mathrm{w}}}{\mathrm{d}h} + nS_{\mathrm{w}}\beta_{\mathrm{w}}\gamma_{\mathrm{w}} \right)$$

$$\times N_J \, \mathrm{d}R \left\{ \frac{\partial h}{\partial t} \right\} + \int_R N_I S_{\mathrm{w}} \frac{\partial N_J}{\partial x_k} \, \mathrm{d}R \left\{ \frac{\partial u_k}{\partial t} \right\}$$

$$= \int_B N_I \mathbf{n} \cdot [\mathbf{K} \cdot \nabla (h+z)] \, \mathrm{d}B + \int_R N_I q \, \mathrm{d}R$$

$$+ \int_R - \nabla N_I \cdot \mathbf{K} \cdot \nabla z \, \mathrm{d}R \quad I, J = 1, 2, 3, \ldots, NN \quad (17)$$

$$\int_R \frac{\partial N_I}{\partial x_j} G \frac{\partial N_J}{\partial x_j} \, \mathrm{d}R\{u_i\} + \int_R \frac{\partial N_I}{\partial x_j} G \frac{\partial N_J}{\partial x_i} \, \mathrm{d}R\{u_j\}$$

$$+ \int_R \frac{\partial N_I}{\partial x_j} \lambda \delta_{ij} \frac{\partial N_J}{\partial x_k} \, \mathrm{d}R\{u_k\} + \int_R - \frac{\partial N_I}{\partial x_j}$$

$$\times S_{\mathrm{w}}\gamma_{\mathrm{w}}\delta_{ij} N_J \, \mathrm{d}R\{h\} = \int_B N_I \sigma_{ij}^{\mathrm{e}} n_j \, \mathrm{d}B + \int_R N_I [nS_{\mathrm{w}}\rho_{\mathrm{w}}$$

$$+ (1-n)\rho_{\mathrm{s}}]^{\mathrm{e}} g_{\mathrm{i}} \, \mathrm{d}R + \int_R \frac{\partial N_I}{\partial x_j} (S_{\mathrm{w}}\gamma_{\mathrm{w}}\delta_{ij} h)^{\circ} \, \mathrm{d}R$$

$$I, J = 1, 2, 3, \ldots, NN \qquad i, j = x, y, z \qquad (18)$$

where $\{\cdot\}$ represents the vector of the unknown variable φ or its time derivative, R is the domain of interest with boundary B, and n_j is the component of the outward unit vector $\mathbf{n}$ normal to the boundary B in the j direction. The finite difference scheme with a time weighting factor ω ($0 \leqslant \omega \leqslant 1$) is then employed to discretize the time derivative terms in equation (17).

Equations (1) and (2) describe initial and boundary value problems. Thus the matrix equations (17) and (18) must be completely constrained by initial and boundary conditions before they are solved. Initial distributions of pressure head and displacement must be prescribed in the entire domain of interest R. The boundary conditions associated with equation (17) and (18) are of the following four types: Dirichlet-type prescribed pressure head $h(t)$, Neumann-type prescribed normal flux to boundary $\mathbf{q}_r(t) = -\mathbf{n} \cdot [\mathbf{K} \cdot \nabla (h+z)]$, Dirichlet-type prescribed displacement in the i direction $u_i(t)$, and Neumann-type prescribed surface traction in the i direction $t_i(t) = \sigma_{ij}^{\mathrm{e}} n_j$. In addition, mixed-type boundary conditions, which are combinations of the Dirichlet and Neumann boundary conditions, are sometimes necessary to treat more realistic situations occurring on the boundary. The variable rainfall–evaporation–seepage and excavation boundary conditions are examples of such mixed-type boundary conditions. The numerical implementations of these two mixed-type boundary conditions were described in detail by Yeh [48] and Kim [49], respectively.

In order to solve the non-linear problem associated with changes in hydraulic properties due to unsaturated water flow and solid skeleton deformation at each time step, the incremental Picard scheme using a non-linear iteration parameter Ω ($0 < \Omega \leqslant 2$) is adopted. For the next non-linear iteration level, the most recently updated nodal values of the dependent variables are used to compute the global coefficient matrices and load vectors in equations (17) and (18). The non-linear iteration is continued until the numerical solution satisfies a specified convergence criterion (tolerance). At each non-linear iteration level, the linearized matrix equation can be solved by one of the iterative nonsymmetric preconditioned conjugate gradient (NSPCG) methods [50]. For this particular study, the ICGMRES (incomplete Cholesky LU decomposed, generalized minimal residual) method is employed among the NSPCG methods in order to solve the linearized matrix equations.

Based on the finite element method described in this section, a numerical model, named COWADE123D [51], has been developed to solve equations (1) and (2) for a variety of fully-coupled hydrogeomechanical phenomena in variably saturated geologic media. The model has been tested by Kim [49] for accuracy by comparing the results with analytical solutions for the following four simplified cases: loading on a top drainage column [17], pumping from a confined aquifer [52], pumping from a leaky aquifer [52], and pumping from an unconfined aquifer [53]. In all the cases, the results show almost perfect or extremely good agreement between the analytical and numerical solutions.

MODEL APPLICATION: A CASE STUDY

The validity of the proposed numerical model may be best illustrated by direct comparison with field measurements taken at a working longwall panel. A coal mine located in Monongalia County, West Virginia, U.S.A. is chosen for this particular study. The mine site lies atop a broad and flat crest at the end of a long steep-sided topographic ridge. As a part of the Eastern Coal Province of the Appalachian Coal Basin, the area contains a significant amount of high-volatile bituminous coal reserves. The longwall mining operation has been applied to extract the Pittsburgh Coal seam. The average thickness of coal extraction is about 1.75 m, and the mining rate is approximately 8 m/day. The study panel is 182 m wide and 2195 m long and is at an approximate average depth of 216 m below the land surface. The site geology and hydrogeology were described in detail by Su and Hasenfus [4] and Hasenfus *et al.* [5].

Geologic and hydrogeologic settings

The geology of the study area is characterized by relatively flat-lying, alternating strata of sandstone, siltstone, shale, claystone, limestone, and coal of Pennsylvanian (Conemaugh Group and Monongahela Group) and Permian (Dunkard Group) ages. The Pittsburgh Coal seam is located at the base of the Monongahela Group. Based on the lithologic and hydrogeologic characteristics, these strata are subdivided into five hydrostratigraphic units as shown in Fig. 1: shallow aquifer I (61 m thick surface soil, sandstone, and sandy shale), aquitard (91.6 m thick shale and claystone with intermittent beds of limestone and sandstone), intermediate aquifer II (63.8 m thick limestone and sandstone), Pittsburgh Coal seam (1.75 m thick coal), and deep aquifer III (more than 200 m thick limestone and sandstone). The intermediate aquifer II and deep aquifer III are hydraulically connected to each other although they are separated by the Pittsburgh Coal seam. The average depth to water table is 10 m from the land surface, and it shows significant seasonal fluctuation up to about 3.5 m. The systematic rock joints in the study area strike mainly N69°W and N19°E and have vertical dips [54]. Another fracture set is developed along the horizontal bedding planes. These three fracture sets form a mutually orthogonal fracture network primarily controlling groundwater movement in the study area. The average annual precipitation rate in the surrounding area during the period 1971–1985 was about 1.28 m/yr [55].

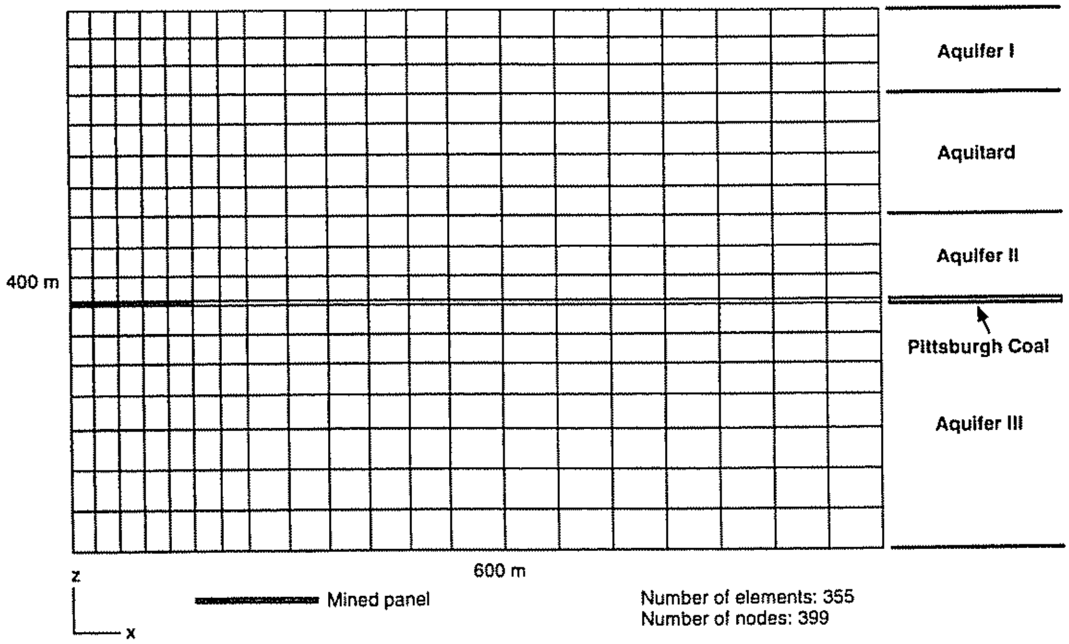

Fig. 1. Geologic cross section of the study area and finite element mesh used in the numerical simulation.

Initial and boundary conditions

Considering the lateral symmetry with respect to the centerline of the panel and assuming plane strain, only the right half portion (600 m × 400 m) of the cross section is taken as a two-dimensional vertical system with a unit thickness (i.e. 1 m) as shown in Fig. 1. Accordingly, two vertical and horizontal fracture sets are considered. Prior to the start of the mining, the initial hydrostatic condition corresponding to the measured water table located 10 m below the land surface is used because an initial distribution of hydraulic head in the study area is not available except for the water table location. Along the left-hand side at $x = 0$ m, no-flow and no-horizontal displacement boundary conditions are applied considering the symmetry, but vertical displacement is allowed. Along the right-hand side at $x = 600$ m, a constant head boundary condition with the hydraulic head ϕ being equal to 10 m below the top surface and a no-horizontal displacement boundary condition are applied, but vertical displacement is allowed. The impermeable bottom surface at $z = 0$ m is fixed vertically, but it is free to move horizontally. The top (land) surface at $z = 400$ m is free to move both vertically and horizontally and is treated as permeable by applying a variable rainfall boundary condition [48] with a rate of 1.28 m/yr to take into account possible changes in infiltration rate cause by the mining. For such a case, the maximum pressure head on the land surface is set equal to its initial pressure head (i.e. -10 m) in order to prevent a possible water table rise up to the land surface during and after the mining period because it is not likely to happen in most real situations. Two different sets of boundary conditions are prescribed along the mined void depending on the time. The simulated mining period is set equal to 3 hr to take into account the instantaneous opening (excavation) of the mined void in the numerical simulation, which in reality is created by a mining rate of 8 m/day and a unit thickness (i.e. 1 m) of the system. During the mining period (simulation time $t \leqslant 3$ hr), no displacement is allowed along the mined void because the mine roof rests on the hydraulic supports. At the same time, a variable seepage boundary condition [48] is also applied to account for possible dewatering (desaturation) around the mined void. For such a case, the maximum pressure head along the mined void is set equal to zero so that no ponding is allowed on the seepage face (mined void), and no water flow is allowed into the surrounding strata from the mined void. After the mining period (simulation time $t > 3$ hr), an excavation boundary condition [49] is applied along the mined void as a combination of prescribed surface traction and displacement boundary conditions. A surface traction boundary condition is first applied to account for collapse due to the overburden load, which is equivalent to the unit weight of overburden material multiplied by its thickness (i.e. 5.64×10^6 N/m^2). Overclosure of the open space (mined void) is then prevented by applying a displacement tolerance as a displacement boundary condition to contacting surfaces between the mine roof and floor. The displacement tolerance is set equal to the height of the mined void (i.e. 1.75 m). The flow boundary condition is not assigned along the mined void because it is completely closed after the mining period in the real situation observed.

Material properties of hydrostratigraphic units and groundwater

Equations (5) and (6) are employed to determine the effect of unsaturated water flow on the unsaturated hydraulic properties, while the deformation-dependencies of porosity and saturated hydraulic conductivity are evaluated by equations (11), (12), (14), and (15). The material properties of the geologic media (hydrostratigraphic units) in the study area are obtained by incorporating all sources of information available for the mine site and surrounding area. These material properties are summarized in Table 1. It is assumed that each hydrostratigraphic unit is initially homogeneous and isotropic. The premining (initial) saturated hydraulic conductivity K_{sat_0} was determined by *in situ* pumping and slug tests [5]. The mechanical properties such as Poisson's ratio ν and the rock matrix modulus E_{matrix} were determined from laboratory uniaxial compressive loading tests [14]. Some of the mechanical properties were extrapolated from the laboratory test results. The solid density ρ_s of each hydrostratigraphic unit was calculated by taking an average of those of typical rocks and minerals that constitute the unit [43]. The *in situ* fracture spacing measured from outcropping rocks ranges from 0.04 to 0.35 m [56]. Accordingly, a uniform initial fracture spacing s_o of 0.2 m is assumed

Table 1. Material properties of the hydrostratigraphic units in the study area

Property	Aquifer I (shallower)	Aquitard	Aquifer II	Pittsburgh Coal	Aquifer III (deeper)
Poisson's ratio, ν (dimensionless)	0.27	0.18	0.20	0.37	0.20
Young's modulus, $E = E_{\mathrm{mass}}$ (N/m^2 = Pa)	2.40×10^9	8.32×10^8	5.14×10^8	1.81×10^8	6.34×10^8
Solid density, ρ_s (kg/m^3)	2.67×10^3	2.63×10^3	2.68×10^3	1.44×10^3	2.70×10^3
Initial saturated hydraulic conductivity, K_{sat_0} (m/s)	2.01×10^{-5}	7.55×10^{-7}	3.91×10^{-6}	2.36×10^{-6}	3.39×10^{-6}
Initial fracture spacing, s_o (m)	0.2	0.2	0.2	0.2	0.2
Initial fracture aperture, b_o (m)	1.70×10^{-4}	5.70×10^{-5}	9.86×10^{-5}	8.33×10^{-5}	9.40×10^{-5}
Initial porosity, n_o (dimensionless)	1.70×10^{-3}	5.70×10^{-4}	9.86×10^{-4}	8.33×10^{-4}	9.40×10^{-4}
Modulus reduction ratio, R_m (dimensionless)	0.5	0.5	0.5	0.5	0.5
Residual water saturation, S_{wr} (dimensionless)	0.07	0.07	0.07	0.07	0.07
Air-entry value, h_a (m)	0.0	0.0	0.0	0.0	0.0
Allowed minimum pressure head, h_b (m)	-5.0×10^1	-5.0×10^1	-5.0×10^1	-5.0×10^1	-5.0×10^1

throughout the entire geologic media. The initial hydraulic fracture aperture b_o can be calculated from the initial saturated hydraulic conductivity K_{sat_o} and fracture spacing s_o by using equation (13) with $u_{fn} = u_{tn} = 0$. The initial porosity n_o can then be estimated by using equations (11) and (12). The modulus reduction ratio R_m of the geologic media was determined to be about 0.5 from the assumed initial fracture spacing s_o of 0.2 m by using a table developed by Ouyang and Elsworth [23] based on the Rock Mass Rating (RMR) system [41]. Then Young's modulus E (=effective rock mass modulus E_{mass}) was calculated from the rock matrix modulus E_{matrix} and modulus reduction ratio R_m by using a relationship (i.e. $E_{mass} = E_{matrix} R_m$), which is implemented in equation (10). Values of the unsaturated hydraulic parameters (S_{wr}, h_a, and h_b) were extrapolated

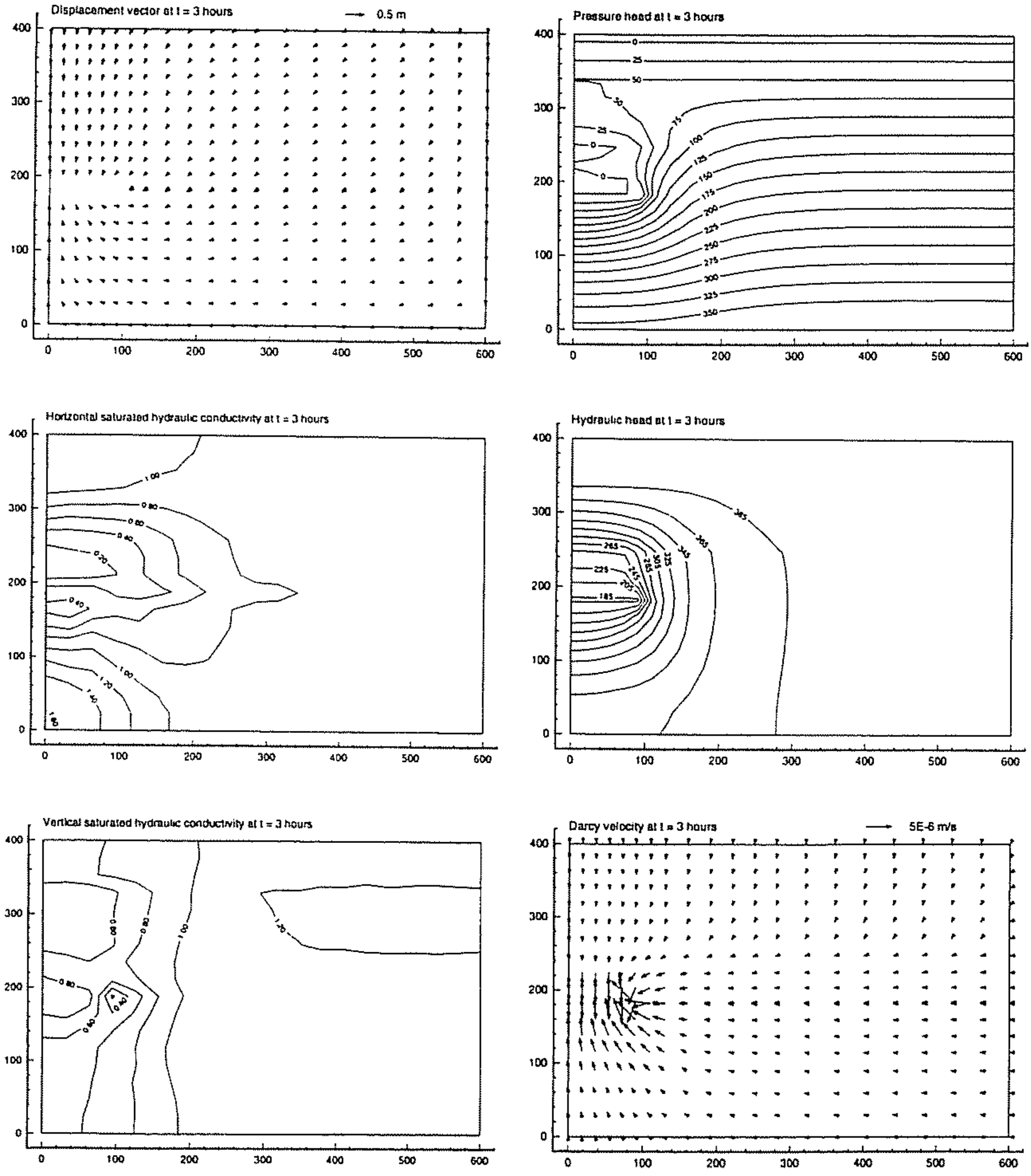

Fig. 2. Spatial distributions of displacement vector, horizontal and vertical saturated hydraulic conductivities, pressure head, hydraulic head, and Darcy velocity at the end of mining (simulation time $t = 3$ hr). The horizontal and vertical saturated hydraulic conductivities are normalized with respect to the initial values, and the null influence contour is represented by a ratio of unity. An unsaturated zone is represented by an area of negative pressure head. The units of displacement vector, pressure head, and hydraulic head are m, and the unit of Darcy velocity is m/s. The units of the horizontal and vertical coordinate axes are m.

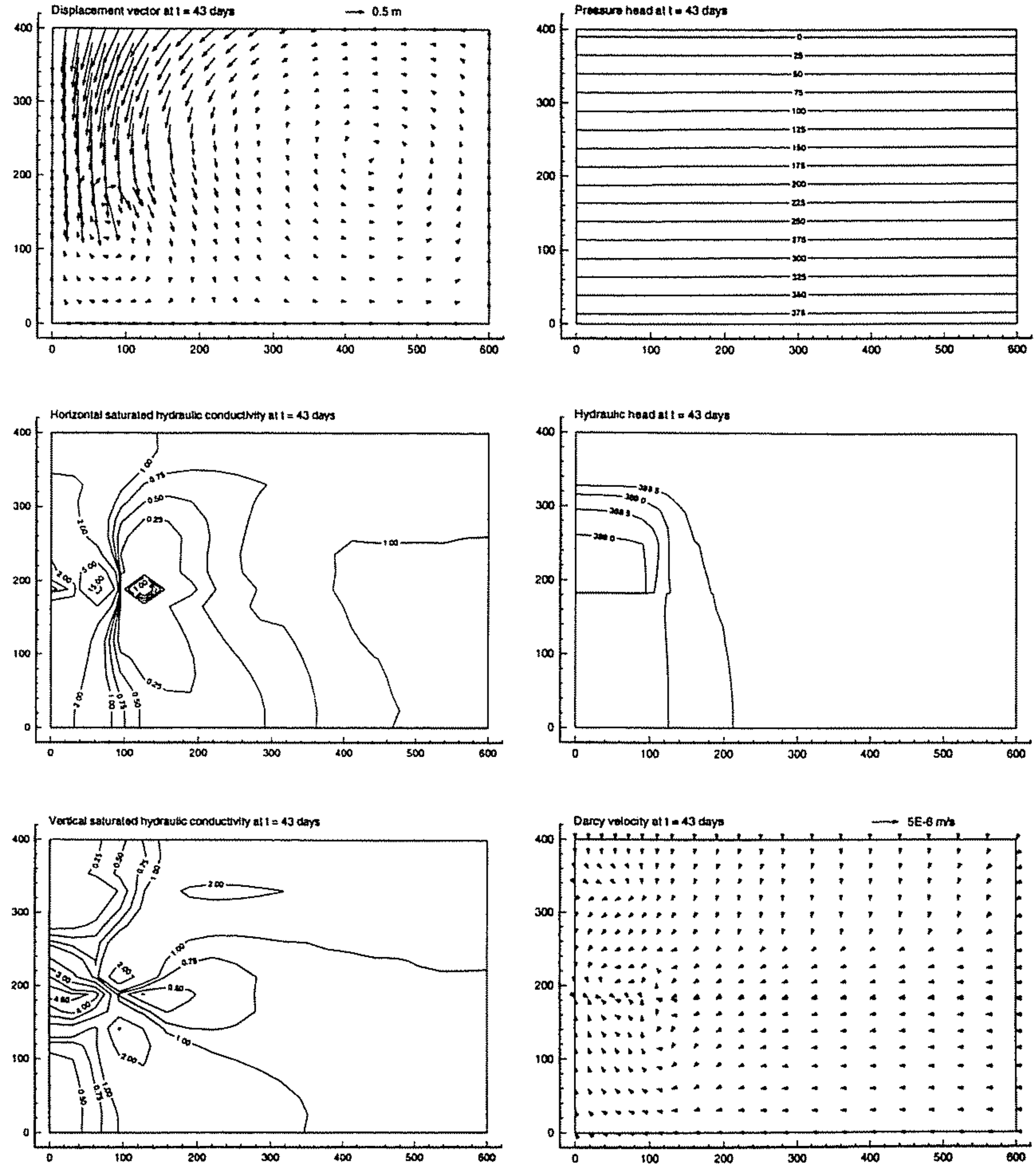

Fig. 3. Spatial distributions of displacement vector, horizontal and vertical saturated hydraulic conductivities, pressure head, hydraulic head, and Darcy velocity at the quasi-steady state after mining (simulation time $t = 43$ days). The horizontal and vertical saturated hydraulic conductivities are normalized with respect to the initial values, and the null influence contour is represented by a ratio of unity. An unsaturated zone is represented by an area of negative pressure head. The units of displacement vector, pressure head, and hydraulic head are m, and the unit of Darcy velocity is m/sec. The units of the horizontal and vertical coordinate axes are m.

from measurement data reported in the literature [32,33]. These values are typical of fractured rock mass. The compressibility of water β_w is set equal to 5.0×10^{-10} m^2/N, and the unit weight of water γ_w is set equal to 9.806×10^3 N/m^3. The dynamic viscosity of water is equal to 1.002×10^{-3} Ns/m^2.

Spatial and temporal discretizations and solution scheme

The domain of interest is discretized into 355 ($=20 \times 18 - 5$) 4-node isoparametric quadrilateral elements of unequal sizes with 399 ($=21 \times 19$) nodes as shown in Fig. 1. The element size is smaller around the mined panel and gradually increases outward. During

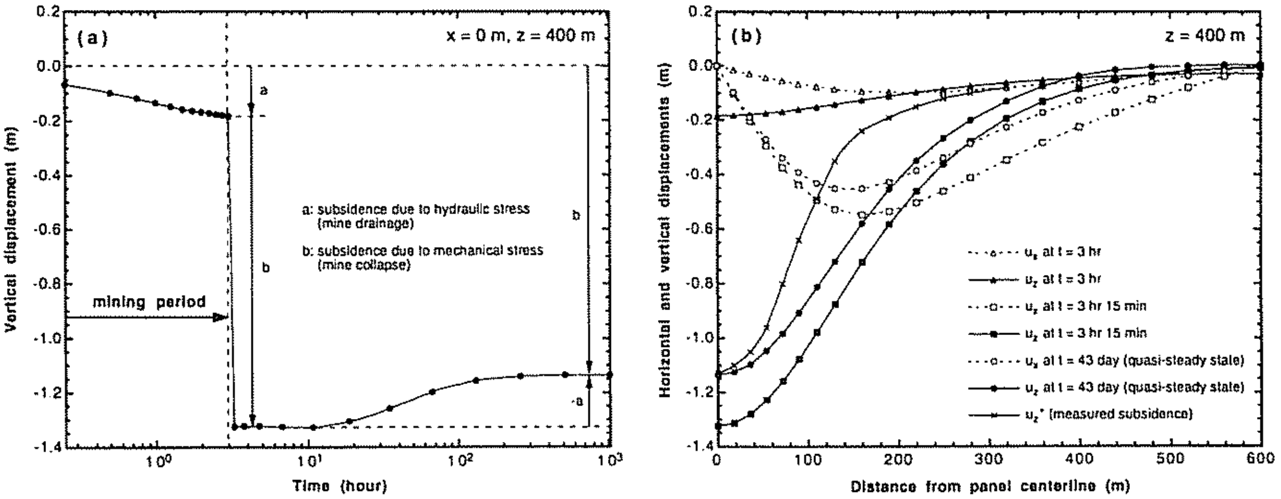

Fig. 4. Temporal changes of (a) vertical displacement at $x = 0$ m, $z = 400$ m and (b) horizontal and vertical displacement profiles on the land surface ($0 \text{ m} \leqslant x \leqslant 600$ m, $z = 400$ m).

the mining period (simulation time $t \leqslant 3$ hr), a constant time step size of 15 min is used. After the mining period (simulation time $t > 3$ hr), the first time step is also 15 min, and the time step size is successively increased by a factor of 2 until it reaches 30,720 min. The total simulation time period is about 43 days (more exactly 3.6963×10^6 sec). The time weighting factor ω is set equal to 1.0 (implicit backward time stepping). The non-linear iteration parameter Ω is set equal to 0.25 (under-relaxation scheme) to prevent numerical oscillation. The convergence criteria (tolerances) for pressure head and displacement are set equal to 10^{-3} m for non-linear iterations and 10^{-4} m for linear iterations, while the linearized matrix equations are solved by the ICGMRES (incomplete Cholesky LU decomposed, generalized minimal residual) method.

Numerical simulation results

The spatial distributions of displacement vector, horizontal and vertical saturated hydraulic conductivities, pressure head, hydraulic head, and Darcy velocity at $t = 3$ hr (at the end of mining) and $t = 43$ days (at the quasi-steady state after mining) are shown in Figs 2 and 3, respectively.

The subsidence (vertical displacement) profile on the land surface drops to its maximum position very quickly as soon as the mined void is closed at $t = 3$ hr 15 min as shown in Fig. 4(a). This mechanically induced deformation as a result of mine roof collapse occurs within 15 min of applying the change in mechanical boundary conditions along the mined void. The computational time step is 15 min, so this dramatic change in the subsidence profile may physically occur somewhat more rapidly (essentially instantaneously). Then it approaches to the final steady state position which is slightly less than the maximum subsidence. This oscillation results from the recovery of water level after the mining period. An adequate match is apparent between measured and predicted final subsidence profiles on the land surface as shown in Fig. 4(b). The predicted final vertical displacement at the panel centerline ($x = 0$ m) is 1.14 m, whereas the measured value is 1.13 m [4]. However, the predicted final subsidence profile shows more extensive ground deformation than that actually measured. This may indicate the presence of heterogeneity within each hydrostratigraphic unit or the mechanical failure of the overburden strata, or may result from neglecting the direct influence of overlying local topography or the existence of unconsolidated soils which are apparently non-linear and inelastic. Whichever of these causes are operative, the difference between the measured and predicted subsidence profiles is not critical. Hence the match can be considered reasonable recognizing that there is no calibration procedure involved in this numerical simulation. Therefore, the results from this numerical analysis are expected to represent the field behavior closely and adequately.

Although each hydrostratigraphic unit is considered to be initially homogeneous and isotropic, a significant heterogeneous and anisotropic hydraulic conductivity field develops as a result of mining (both drainage and collapse). During the mining period (Fig. 2), the greatest decreases in both horizontal and vertical saturated hydraulic conductivities develop in the area around the panel where large compressional deformation results from mine drainage without mine collapse because the mined void remains open owing to the hydraulic supports. Horizontal saturated hydraulic conductivity increases vertically from the panel because it is modified by vertical deformation, while vertical saturated hydraulic conductivity increases horizontally from the panel because it is controlled by horizontal deformation. However, after the mining period (Fig. 3), a totally different saturated hydraulic conductivity field is developed due to mine collapse. As anticipated, the greatest increases in horizontal and vertical saturated hydraulic conductivities occur in the area immediately over the panel where large extensional deformation results from mine collapse. The zone of horizontal saturated hydraulic conductivity enhancement develops vertically above and below the panel and extends to the

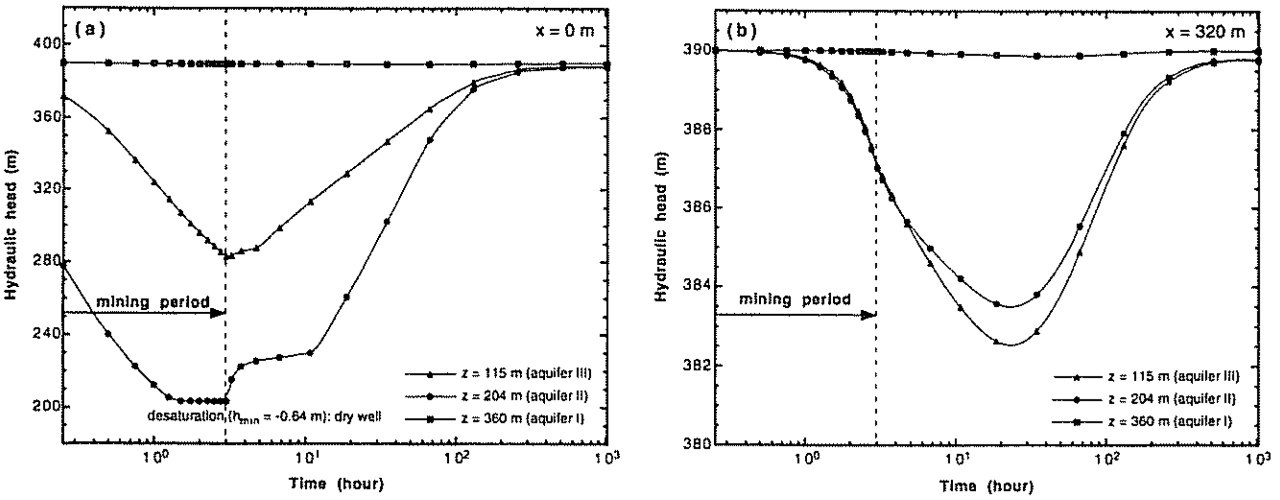

Fig. 5. Temporal changes of hydraulic head at (a) $x = 0$ m and (b) $x = 320$ m in the shallow aquifer I ($z = 360$ m), intermediate aquifer II ($z = 204$ m), and deep aquifer III ($z = 115$ m).

land surface as a result of high vertical extensional strain toward the panel. Another small isolated enhancement zone of horizontal saturated hydraulic conductivity is also formed outside the panel edge. The enhancement of vertical saturated hydraulic conductivity is, however, limited to a narrow region around the panel. This enhancement zone appears coincident with the area of high horizontal extensional strain that develops at the abutment and slopes upward and downward at an angle of about 45°. The same longwall mining-modified hydraulic conductivity fields were predicted from other numerical simulations [22,23,25]. Postmining borehole packer tests conducted in the study area also confirmed both increasing and decreasing saturated hydraulic conductivities relative to premining values as a result of strata movement and dilation of existing joints and bedding planes [5].

Two desaturation zones are formed between the mined void and the aquitard within the intermediate aquifer II during the mining period (Fig. 2) and are resaturated after the mining period (Fig. 3). As shown in Fig. 5(a), the hydraulic head in the shallow aquifer I is relatively unaffected by longwall mining owing to the presence of the underlying relatively impermeable aquitard, whereas the water levels in the intermediate aquifer II and deep aquifer III show significant declines. The water level in the intermediate aquifer II ($z = 204$ m) even becomes negative during the mining period. The same trends (but different magnitudes) were observed in six monitoring wells, which were located directly over the study panel [5]. Water levels in wells W2, W4, and W6 completed in the shallow aquifer I declined by less than 3 m and then recovered to near their premining levels. However, wells W1, W3, and W5 completed in the intermediate aquifer II showed significant drawdown, more than 120 m, and sometimes went dry, i.e. desaturated. Ultimately, they showed very slow recovery toward the premining levels. These water level responses suggest that, in the study area, the shallow aquifer I is hydraulically isolated from the mined void by the underlying less permeable aquitard, while the intermediate aquifer II and deep aquifer III remain hydraulically connected to the mined void. Furthermore, the water levels at $x = 320$ m in the intermediate aquifer II and deep aquifer III continue to decline even after the mining period but eventually recover to near their premining levels as shown in Fig. 5(b).

CONCLUSIONS

On the basis of an equivalent porous elastic continuum representation and corresponding poroelastic theory, a fully-coupled hydrogeomechanical model for saturated–unsaturated groundwater flow in deforming geologic media and its numerical formulation have been presented. Unsaturated hydraulic parameters necessary for its application were selected from formulations available in the literature. The explicit coupling between the groundwater flow field and the solid skeleton deformation field is achieved by simultaneously solving the mathematical governing equations for groundwater flow and solid skeleton deformation. The implicit coupling between these two fields is also accomplished by considering the effects of both unsaturated water flow and solid skeleton deformation on the hydraulic properties such as water content and hydraulic conductivity. In addition to the implicit coupling caused by unsaturated water flow, the other implicit coupling caused by solid skeleton deformation is also important because it may produce hydraulic heterogeneity and anisotropy in a geologic medium affecting the groundwater flow field even when the system is in a fully saturated condition. Thus a physically based constitutive model has also been proposed to account for the deformation (strain)-dependencies of porosity and saturated hydraulic conductivity of the fractured media. To evaluate fully-coupled strata deformation and groundwater flow induced by underground longwall mining and to understand their hydrogeomechanical nature, the numerical model has been applied to a real mine site. A series of consistent trends is evident, to a certain extent, between the results from the simulation and those from the field measurements. Although the numerical simulation results presented in this paper will not apply to all underground longwall mines because of differences in site-specific hydrogeological and geomechanical settings, the methodology described herein may find some useful applications in many longwall mining projects. Further development of the numerical model (e.g shear and tension failures) and field application are encouraged to better fit the observed field behavior.

Acknowledgements—This work was supported in part by the National Mine Land Reclamation Center (NMLRC) of the West Virginia University under grants CO388026 and G114-5154, and in part by a fellowship from the Mining and Mineral Resources Research Institute (MMRRI) of the Pennsylvania State University. The authors would also like to thank two anonymous reviewers for their valuable and constructive comments.

Accepted for publication 9 July 1997.

REFERENCES

1. Whittaker B. N., Singh R. N. and Neate C. J. Effect of longwall mining on ground permeability and subsurface drainage. In *Mine Drainage* (Edited by Argall Jr, G. O. and Brawner C. O.), pp. 161–183. Miller Freeman Publications, San Francisco (1979).
2. Hill J. G. and Price D. R. The impact of deep mining on an overlying aquifer in western Pennsylvania. *Ground Water Monitor. Rev.* **3**, 138–143 (1983).
3. Booth C. J. Strata-movement concepts and the hydrogeological impact of underground coal mining. *Ground Water* **24**, 507–515 (1986).
4. Su D. H. W. and Hasenfus G. J. Field measurements of overburden and chain pillar response to longwall mining. *Proceedings of the 6th International Conference on Ground Control in Mining* (Edited by Peng S. S.), Mogantown, West Virginia, pp. 296—311 (1987).
5. Hasenfus G. J., Johnson K. L. and Su D. W. H. A hydrogeomechanical study of overburden aquifer response to longwall mining. *Proceedings of the 7th International Conference on Ground Control in Mining* (Edited by Peng S. S.), Morgantown, West Virginia, pp. 149–162 (1988).
6. Booth C. J. and Spande E. D. Potentiometric and aquifer property changes above subsiding longwall mine panels, Illinois Basin Coalfield. *Ground Water* **30**, 362–368 (1992).
7. Donohue T. D. A. and Parizek R. R. Evaluation of the long term impact of domestic and farm groundwater supplies under Pennsylvania longwall mining conditions. *Proceedings of the International Land Reclamation and Mine Drainage Conference and the 3rd International Conference on the Abatement of Acidic Drainage*, Pittsburgh, Pennsylvania, Vol. 4, pp. 180–189 (1994).
8. Owili-Eger A. S. C. Mathematical modelling and digital simulation of soil-aquifer groundwater motion and mine water drainage. Ph.D. dissertation, 288 pp., Pennsylvania State University, University Park, Pennsylvania (1975).
9. Stoner J. D. Probable hydrologic effects of subsurface mining. *Ground Water Monitor. Rev.* **3**, 128–137 (1983).
10. Booth C. J. A numerical model of groundwater flow associated with an underground coal mine in the Appalachian Plateau. Ph.D. dissertation, 458 pp., Pennsylvania State University, University Park, Pennsylvania (1984).
11. Kim J. M. Numerical simulation of hydrogeological impacts of underground coal mining. Reserach Proposal, 22 pp., Department of Geosciences, Pennsylvania State University, University Park, Pennsylvania (1993).
12. Fitzpatrick D. J., Reddish D. J. and Whittaker B. N. Studies of surface and sub-surface ground movements due to longwall mining operations. *Proceedings of the 2nd Workshop on Surface Subsidence Due to Underground Mining* (Edited by Peng S. S.), Morgantown, West Virginia, pp. 68–77 (1986).
13. Agioutantis Z., Karmis M. and Jarosz A. Prediction of surface subsidence and strain in the Appalachian Coalfields using numerical methods. *Proceedings of the 7th International Conference on Ground Control in Mining* (Edited by Peng S. S.), Morgantown, West Virginia, pp. 95–100 (1988).
14. Su D. H. W. Finite element modeling of surface subsidence induced by underground coal mining. *Proceedings of the 3rd Workshop on Surface Subsidence Due to Underground Mining* (Edited by Peng S. S.), Morgantown, West Viginia, pp. 32–46 (1992).
15. Thin I. G. T., Pine R. J. and Trueman R. Numerical modelling as an aid to the determination of the stress distribution in the goaf due to longwall coal mining. *Int. J. Rock Mech. Min. Sci. & Geomech. Abstr.* **30**, 1403–1409 (1993).
16. Yang G., Chugh Y. P., Yu Z. and Salamon M. D. G. A numerical approach to subsidence prediction and stress analysis in coal mining using a laminated model. *Int. J. Rock Mech. Min. Sci. & Geomech. Abstr.* **30**, 1419–1422 (1993).
17. Biot M. A. General theory of three-dimensional consolidation. *J. Appl. Phys.* **12**, 155–164 (1941).
18. Verruijt A. Elastic storage of aquifers. In *Flow Through Porous Media* (Edited by De Wiest R. J. M.), pp. 331–376. Academic Press, New York (1969).
19. Safai N. M. and Pinder G. F. Vertical and horizontal land deformation in a desaturating porous medium. *Adv. Water Resour.* **2**, 19–25 (1979).
20. Noorishad J., Mehran M. and Narasimhan T. N. On the formulation of saturated–unsaturated fluid flow in deformable porous media. *Adv. Water Resour.* **5**, 61–62 (1982).
21. Girrens S. P., Anderson C. A., Bennett J. G. and Kramer M. Numerical prediction of subsidence with coupled geomechanical–hydrological modeling. *Proceedings of the Workshop on Surface Subsidence Due to Underground Mining* (Edited by Peng S. S. and Harthill M.), Morgantown, West Virginia, pp. 63–70 (1981).
22. Bai M. and Elsworth D. Modeling subsidence and groundwater flow due to underground mining. *Proceedings of the 34th Annual Meeting of the Association of Engineering Geologists*, Chicago, Illinois, pp. 981–990 (1991).
23. Ouyang Z. and Elsworth D. Evaluation of grondwater flow into mined panels. *Int. J. Rock Mech. Min. Sci. & Geomech. Abstr.* **30**, 71–79 (1993).
24. Bai M. and Elsworth D. Modeling of subsidence and stress-dependent hydraulic conductivity for intact and fractured porous media. *Rock Mech. Rock Eng.* **27**, 209–234 (1994).
25. Elsworth D., Liu J. and Ouyang Z. Some approaches to determine the potential influence of longwall mining on groundwater water resources. *Proceedings of the International Land Reclamation and Mine Drainage Conference and the 3rd International Conference on the Abatement of Acidic Drainage*, Pittsburgh, Pennsylvania, Vol. 4, pp. 172–179 (1994).
26. Oda M. An equivalent continuum model for coupled stress and fluid flow analysis in jointed rock masses. *Water Resour. Res.* **22**, 1845–1856 (1986).
27. Zhu W. and Wang P. Finite element analysis of jointed rock masses and engineering application. *Int. J. Rock Mech. Min. Sci. & Geomech. Abstr.* **30**, 537–544 (1993).
28. Pariseau W. G. Equivalent properties of a jointed Biot material. *Int. J. Rock Mech. Min. Sci. & Geomech. Abstr.* **30**, 1151–1157 (1993).
29. Brooks R. H. and Corey A. T. Hydraulic properties of porous media. Hydrology Papers 3, 27 pp., Colorado State University, Fort Collins, Colorado (1964).
30. Van Genuchten M. Th. A closed-form equation for predicting the hydraulic conductivity of unsaturated soils. *Soil Sci. Soc. Amer. J.* **44**, 892–898 (1980).
31. Russo D. Determining soil hydraulic properties by parameter estimation: On the selection of a model for the hydraulic properties. *Water Resour. Res.* **24**, 453–459 (1988).
32. Peters R. R., Klavetter E. A., Hall I. J., Blair S. C., Heller P. R. and Gee G. W. Fracture and matrix hydrologic characteristics of tuffaceous materials from Yucca Mountain, Nye County, Nevada. Report SAND-84-1471, 184 pp., Sandia National Laboratories, Albuquerque, New Mexico (1984).
33. Reitsma S. and Kueper B. H. Laboratory measurement of capillary pressure–saturation relationships in a rock fracture. *Water Resour. Res.* **30**, 865–878 (1994).
34. Huyakorn P. S., Thomas S. D. and Thompson B. M. Techniques for making finite elements competitive in modeling flow in variably saturated porous media. *Water Resour. Res.* **20**, 1099–1115 (1984).

35. Gangi A. F. Variation of whole and fractured porous rock permeability with confining pressure. *Int. J. Rock Mech. Min. Sci. & Geomech. Abstr.* **15**, 249–257 (1978).
36. Witherspoon P. A., Wang J. S. Y., Iwai K. and Gale J. E. Validity of cubic law for fluid flow in a deformable rock fracture. *Water Resour. Res.* **16**, 1016–1024 (1980).
37. Tsang Y. W. and Witherspoon P. A. Hydromechanical behavior of a deformable rock fracture subject to normal stress. *J. Geophys. Res.* **86**, 9287–9298 (1981).
38. Walsh J. B. Effect of pore pressure and confining pressure on fracture permeability. *Int. J. Rock Mech. Min. Sci. & Geomech. Abstr.* **18**, 429–435. (1981).
39. Raven K. G. and Gale J. E. Water flow in a natural rock fracture as a function of stress and sample size. *Int. J. Rock Mech. Min. Sci. & Geomech. Abstr.* **22**, 251–261 (1985).
40. Chernyshev S. N. and Dearman W. R. *Rock Fractures*, p. 272. Butterworth-Heinemann, London (1991).
41. Bieniawski Z. T. *Engineering Rock Mass Classifications*, p. 251. Wiley, New York (1989).
42. Snow D. T. Anisotropic permeability of fractured media. *Water Resour. Res.* **5**, 1273–1289 (1969).
43. Goodman R. E. *Introduction to Rock Mechanics*, p. 478. Wiley, New York (1980).
44. Parsons R. W. Permeability of idealized fractured rock. *Soc. Pet. Eng. J.* **6**, 126–136 (1966).
45. Snow D. T. Rock fracture spacings, openings, and porosities. *J. Soil Mech. Found. Div. Amer. Soc. Civil Eng.* **94**, 73–91 (1968).
46. Huyakorn P. S. and Pinder G. F. *Comutational Methods in Subsurface Flow*, p. 473. Academic Press, New York (1983).
47. Zienkiewicz O. C. and Taylor R. L. *The Finite Element Method*, 4th edn, Vol. 1, p. 648 & Vol. 2, p. 807. McGraw-Hill, New York (1991).
48. Yeh G. T. FEMWATER: A finite element model of water flow through saturated–unsaturated porous media—first revision. Report ORNL-5567/R1, 258 pp., Oak Ridge National Laboratory, Oak Ridge, Tennessee (1987).
49. Kim J. M. A fully-coupled model for saturated–unsaturated fluid flow in deformable porous and fractured media. Ph.D. dissertation, 201 pp., Pennsylvania State University, University Park, Pennsylvania (1996).
50. Oppe T. C., Joubert W. D. and Kincaid D. R. NSPCG user's guide version 1.0: A package for solving large sparse linear systems by various iterative methods. Report CNA-216, 82 pp., Center for Numerical Analysis, University of Texas, . Austin, Texas (1988).
51. Kim J. M. COWADE123D: A finite element model for fully-coupled saturated–unsaturated water flow in deforming one-, two-, and three-dimensional porous and fractured media. Report HGL-1995-9, 254 pp., Hydrogeology Laboratory, Department of Geosciences, Pennsylvania State University, University Park, Pennsylvania (1995).
52. Bear J. and Corapcioglu M. Y. Mathematical model for regional land subsidence due to pumping, 2. Integrated aquifer subsidence equations for vertical and horizontal displacements. *Water Resour. Res.* **17**, 947–958 (1981).
53. Corapcioglu M. Y. and Bear J. A mathematical model for regional land subsidence due to pumping, 3. Integrated equations for a phreatic aquifer. *Water Resour. Res.* **19**, 895–908. (1983).
54. Diamond W. P., McCulloch C. M. and Bench B. M. Use of surface joints and photo-linear data for predicting subsurface coal cleat orientation. U.S. Bureau of Mines Report of Investigations 8120, 13 pp. (1976).
55. U.S. National Oceanic and Atmospheric Administration. *Climatological data: West Virginia*, Asheville, North Carolina (published annually, 1971–1985).
56. Kohl W. R. Jointing in outcropping rocks of Pennsylvanian age, central Greater Pittsburgh region, Pennsylvania. U.S. Geological Survey Open-File Report 80-23, 16 pp. (1980).